Demonstration of a 13-keV Kr *K*-shell x-ray source at the National Ignition Facility

K. B. Fournier,[1] M. J. May,[1] J. D. Colvin,[1] M. A. Barrios,[1] J. R. Patterson,[1] and S. P. Regan[2]

[1]*Lawrence Livermore National Laboratory, P.O. Box 808, L-481, Livermore, California 94550, USA*
[2]*Laboratory for Laser Energetics, University of Rochester, Rochester, New York 14623, USA*

We report 3% conversion efficiency of laser energy into Kr *K*-shell ($\approx$13 keV) radiation, consistent with theoretical predictions. This is $\approx$10$\times$ greater than previous work. The emission was produced from a 4.1-mm-diameter, 4-mm-tall gas pipe target filled with 1.2 or 1.5 atm of Kr gas. 160 of the National Ignition Facility laser beams deposited $\approx$700 kJ of 3ω light into the target in an $\approx$140 TW, 5.0-ns-duration square pulse. The Dante diagnostics measured $\approx$5 TW into 4π solid angle of $\geqslant$12 keV x rays for $\approx$4 ns, which includes both continuum emission and flux in the Kr He$_\alpha$ line at 13 keV.

PACS number(s): 52.50.Jm, 52.25.Os, 52.70.La

There have been many efforts in the last decade to create underdense, laser-driven plasma radiation sources. An effort to make targets that are solid at room temperature, but with densities in the range of those from gas targets has led to much research into metal-doped silica aerogel targets [1–4] and other metallic-oxide nanostructured materials [5]. Similarly, ultra-low-density, elementally pure plasma radiation sources have been formed by preexploding thin metallic foils with a laser prepulse before delivering the main pulse [6,7]. Calculations have shown that the multi-keV emissivity of highly charged mid- and high-*Z* ions in these plasmas is a strong function of temperature, with a different optimum temperature in different spectral bands [8].

High yield x-ray sources are required for large fluence-area-product exposures with a high degree of uniformity across the face of a test article. Increasing efficiency allows higher yields from targets for a fixed laser energy. Higher yields are necessary to get uniform irradiation with sufficient dose over macroscopic test objects at distances of tens of centimeters.

Lasers propagate through underdense targets, where underdense means the target plasma's electron density is less than 25% of the laser's critical density for Raman scattering [9], $n_e \leqslant 0.25 n_{cr}$. The laser's critical density n_{cr} is given by $1.1 \times 10^{21}/\lambda^2$ where λ is the laser's wavelength in microns; $n_{cr} \approx 9 \times 10^{21}$ cm^{-3} for National Ignition Facility's (NIF's) 0.351 μm laser beams. At pressures around 1 atm, gas targets produce plasmas below $0.25 n_{cr}$, thus, nearly all the laser's energy is absorbed in the gas without losses due to ablation or hydrodynamic motion of solid material [10,11]. In addition, gas targets can be chemically pure, maximizing the number of atoms or ions of interest for the desired x-ray emitter. In this article we report a demonstration of an order-of-magnitude enhancement of laser-to-x-ray conversion efficiency (CE) at 13 keV from Kr gas-filled targets and a record for both the flux and total energy emitted by a 13 keV source.

We have recently demonstrated [12] a 30% enhancement of the laser-to-x-ray CE for $\approx$4.5 keV x rays from Xe targets at $0.1 n_{cr}$ driven by 70 TW of laser power at the NIF [13]. The NIF experiments used more than 7$\times$ the laser energy and $\approx$4$\times$ the laser power available in previous Xe experiments [10,11] at older lasers. The result was more optimal conditions for Xe *L*-shell x-ray production in the NIF experiments [14]. There have been a few previous experiments [15–17] to measure Kr

K-shell (13 keV) radiation at the OMEGA laser [18]. Some of us were involved in campaigns in 2001 and 2002 at the OMEGA laser that measured Kr *K*-shell yield from targets driven with $\approx$20 TW of laser power; laser-to-x-ray CEs of 0.2%–0.5% into x rays with energies $\geqslant$10 keV were measured for targets filled to 1.5 and 1.2 atm, respectively [17]. In 2006, OMEGA experiments measured an electron temperature of $\approx$3 keV at the center of Kr gas-bag plasmas [19]. The present experiments used $\approx$25$\times$ more laser energy than previous experiments and have created near-optimal conditions for Kr *K*-shell x-ray emission. This article experimentally demonstrates that the x-ray environment generated on NIF with a Kr gas-filled target, irradiated with 0.7 MJ of laser energy, achieves a laser-to-x-ray conversion efficiency into Kr *K*-shell emission of $\approx$3%; this is an order-of-magnitude increase over the OMEGA results.

The targets for experiments at NIF were thin-walled (40 μm), 4-mm-long, 4.1-mm-inner-diameter, epoxy (C$_{40}$H$_{51}$N$_2$O$_7$, $\rho = 1.185$ g/cm^3) pipes designed to transmit x rays with energies > 3 keV. Pictures of identical targets are shown in Fig. 1 of Ref. [12]. The targets were filled with 1.2 or 1.5 atm of Kr gas, which was chosen to create a plasma with an electron density $\approx$0.1 or $0.13 n_{cr}$, respectively, assuming an ionization state of Kr^{34+}. The density in the target plasma is computed as $n_{Kr} = (N_{Kr}/V) = \frac{P}{RT}$, where n_{Kr} is the molar density of Kr atoms, N_{Kr} is the number of mols of Kr atoms in the target gas fill, V is the target volume, P is the target pressure, R is the ideal gas constant, and T is the preshot temperature of the target gas in Kelvin. The electron density is then found by $n_e = N_{Av} \langle Z \rangle n_{Kr}$, where $\langle Z \rangle$ represents the average ion charge, and N_{Av} is Avogadro's number. The gas-pipe targets had fill pressures that were measured to be within 1% of the requested pressure at shot time.

These experiments used 160 of NIF's 192 laser beams, divided symmetrically between top and bottom. The beams were oriented in three cones at 30°, 44.5°, and 50° with respect to the target's vertical axis. The outer beam cones (44° and 50°) were pointed 500 μm inside the gas pipe; the inner cone beams were pointed 800 μm outside the gas pipe and diverged into the target's fill gas. For these two shots, the laser delivered $\approx$700 kJ of 351 nm (3ω) light in a 5 ns flattop pulse at a peak power of $\approx$140 TW. The 3ω intensity profile of all beams was smoothed by the NIF ignition-campaign continuous phase
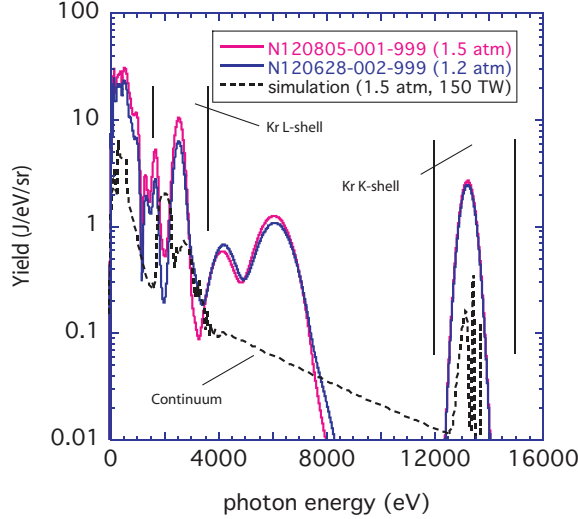
FIG. 1. (Color online) Spectral reconstruction of time-integrated x-ray emission from the 1.2 [blue (dark gray)] and 1.5 atm [magenta (light gray)] Kr targets. The Dante-1 low-energy flux is strongly dominated by unfiltered emission from the target's LEH. Also shown is a simulated spectrum (dashed line, arbitrary units) from the LASNEX code.

plates [20]. Laser parameters for these experiments, and x-ray and optical measurements of target energy, are reported in Table I.

Figure 1 shows the reconstructed x-ray emission from the target as measured with the NIF Dante-1 diagnostic [21,22]. The Dante-1 and Dante-2 [21] are 18 channel, filtered-diode arrays that are installed at the NIF laser facility. Typically the Dantes can record emission from 100 to 20 keV with spectral

TABLE I. Table of measured laser energy, power, and optical backscatter, as well as resulting x-ray yields for the two shots in this campaign.

Parameter	N120628-002	N120805-001
Kr gas pressure (atm)	1.2	1.5
Measured laser power (TW)	136.5	142.9
Measured laser energy (kJ)	683.5	708.3
Backscatter (%)	12.3 ± 2.21	7.6 ± 1.37
L-shell results		
Dante-1 yield (kJ/sr)[a]	3.6 ± 0.1	5.8 ± 0.2
Dante-2 yield (kJ/sr)[a]	4.5 ± 0.2	5.7 ± 0.2
Dante-1 CE (%)	6.6	10.2
Simulation CE (%)[a]	15.9	19.0
K-shell results		
Dante-1 yield (kJ/sr)[b]	1.5 ± 0.1	1.6 ± 0.1
Dante-2 yield (kJ/sr)[b]	1.6 ± 0.1	1.7 ± 0.1
Dante-1 CE (%)	2.8	2.9
Simulation CE (%)[c]	2.0	2.1
SS-II CE in He$_\alpha$ (%)[d]	2.5 ± 1.2	2.9 ± 1.4

[a]Energy in band 1.5–3.5 keV.

[b]Energy in band 8–20 keV.

[c]Energy in band 9–34 keV.

[d]Energy in band 12.5–13.2 keV.

resolving power ($E/\Delta E$) of 5–10. The Dante-1 and Dante-2 systems have views of the target at 37° and 64°, respectively, from the target's cylindrical axis. Thus Dante-1's measurement of (particularly low-energy) flux from the target is dominated by unfiltered emission from the laser entrance hole (LEH) compared to Dante-2's. The Dante signals are reconstructed by algorithms [23,24] that use the measured voltages, the filter transmission, x-ray diode response, and the solid angle of the view of each channel. The Dante calibrations for the whole-system photometric response of each channel are believed to be accurate to between ±5 and 10%. The Kr *L*-shell flux is seen to be directionally dependent, sensitive to how much of the gas pipe is included in the detector's view. A simulated spectrum from the LASNEX/DCA model discussed below is also plotted (thin black line) to allow the reader to see overlap of the calculated photon energies of the identified features and the positions of features resulting from the Dante unfold. For example, we define the *L*-shell band as the spectral region between 1.5 and 3.5 keV based on the simulation; the large bumps in the unfolded data at ≈4.5 and 6.5 keV are artifacts of how the unfold distributes the energy in the continuum emission from the target. The *L*-shell yield [$1.5 \leqslant h\nu(\text{keV}) \leqslant 3.5$] is 5.80 ± 0.22 kJ/sr from the 1.5 atm target, yielding a 10.2% laser-to-x-ray CE.

Time histories of Kr x-ray emission are shown in Fig. 2 for all energies (left) and specifically for the *K*-shell emission (right). The broadband flux (left panel) displays an ≈40% difference between the Dante-1 and Dante-2 measurements. Most of this difference is in the 4–6 keV range where Dante-2 is missing channel coverage. The broadband peak flux from the 1.5 atm target is ≈50% greater than the yield from the 1.2 atm target, a difference that is somewhat greater than what is expected based on previous results [19]. The broadband flux shown in the left panel of Fig. 2 is seen to extend in time beyond the laser pulse by several nanoseconds. This is a result of the recombination of the Kr ions through the *L*- and *M*-shell charge states as the plasma cools.

The *K*-shell flux is measured specifically with a channel that records emission at > 8 keV. The unfold routine was configured to assume all the flux was emitted around the He/H-like *K*-shell lines. The *K*-shell flux measurements for the Dante-1 and Dante-2 lines of sight agree to within 5% for each Kr target, indicating the *K*-shell emission from the source is isotropic. The *K*-shell yield from the 1.5 atm target is 7% greater than the yield from the 1.2 atm target, less than the uncertainty for the measurements (see Table I). This pressure dependence for *K*-shell emission is consistent with previous observations [17,19], and predictions by state-of-the-art radiation-hydrodynamics modeling [14].

The *K*-shell emission decays away shortly after the end of the laser pulse, due to the higher plasma temperatures required to produce *K*-shell ions. For applications that need x-ray flux in a specific energy range, or that have requirements for isotropic emission, the experimenter must keep in mind the different temporal characteristics of the soft *L*-shell radiation and the hard *K*-shell radiation.

In order to quantify the laser energy coupled to the plasma radiation source, laser energy reflected from the target by laser-driven plasmas instabilities (LPI) is measured, as well as the energy carried away by high-energy electrons created
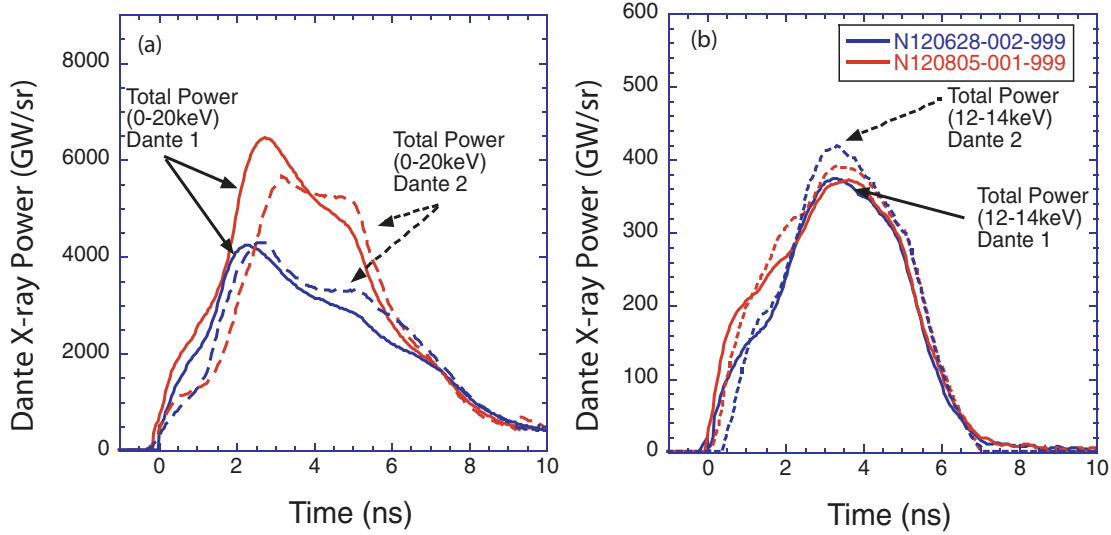
FIG. 2. (Color online) Measured x-ray fluxes for (a) energies 0–20 keV and (b) *K*-shell energies 12–14 keV for both the 1.2 (blue, dark gray traces) and 1.5 atm (magenta, light gray traces) Kr targets. The Dante-1 measurements are shown by solid lines; the Dante-2 measurements by dashes.

by laser-plasma-wave interactions. The hot-electron energy content is negligible and is ignored in the analysis. The conversion efficiency numbers in Table I are *not* adjusted for energy lost by LPI or hot electrons; the CE numbers are given relative to the full laser-system energy delivered to the target. The NIF full-aperture backscatter system [25] and near-backscatter imagers [26] measured 12.3% of the incident light reflected for all beams for the 1.2 atm target when summed over stimulated Brillouin scattering (SBS) and stimulated Raman scattering (SRS) channels [9], and 7.6% for the 1.5 atm target. These numbers represent a beam-weighted average of measurements made on one 50° beam (64 of the 160 beams used) and one 30° beam (32 of the 160 beams used) extrapolated to the full suite of 160 beams. It is assumed losses on the 50° beams (64 of 160) are the same as for the 44.5° beams. Previous observations show that SBS losses decrease for increasing plasma density (pressure), and correspondingly, SRS losses increase. The current data follow these trends [2,12,19].

Spectroscopic data on Kr *K*-shell emission were also taken with the SuperSnout II (SS-II) spectrometer [27]. The SS-II is a four-channel, elliptically-bent-crystal spectrometer providing spectral coverage in the 6–16 keV x-ray range. This time-integrated, one-dimensional (1D) imaging spectrometer viewed the x-ray source target from the north pole of the NIF chamber, through the LEH within 2° of the cylindrical symmetry axis. The SS-II combines a slit aperture with a 100-μm width and a pentaerythritol Bragg crystal to record 1D spectral images of the target with a spectral resolving power of 300–800 [27]. The accuracy of the SS-II photometric calibration is $\pm$50%. Emission line and continuum data measured from the highest energy SS-II channel are plotted in Fig. 3. The photometric response of the crystals is known from laboratory calibrations [28]. The response of the instrument (crystals, filters, and image-plate detector) is used to convert the photostimulated luminescence

signals read from the plate (fade corrected) into x-ray yield. The estimated conversion efficiencies for the 1.2 and 1.5 atm shots are listed in Table I.

We expected the Kr *K*-shell x-ray conversion efficiency to be about 20 times higher for the NIF targets than for equivalent OMEGA-scale targets. We first approximate the output *K*-shell power density by balancing the collisional excitation rate with the radiative decay rate. Following Back *et al*. [10], we assume for simplicity that all the *K*-shell emission comes from ions at the same ionization level, and then including induced emission and absorption in the energy-balance equation [29] we can write

$$P_K \cong (\text{const}) \frac{n_e^2}{\langle Z \rangle} \frac{\exp(-h\nu/kT_e)}{(kT_e)^{1/2}}, \tag{1}$$
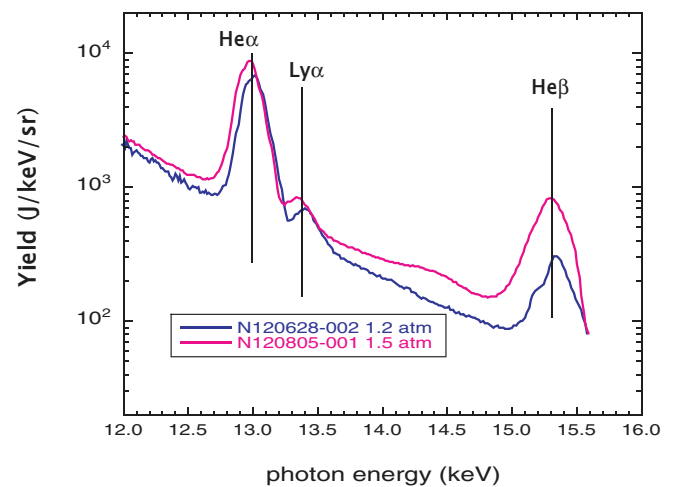
FIG. 3. (Color online) Measured Kr *K*-shell spectra from NIF shot N120805-001 (magenta, light gray) and N120628-002 (blue, dark gray).
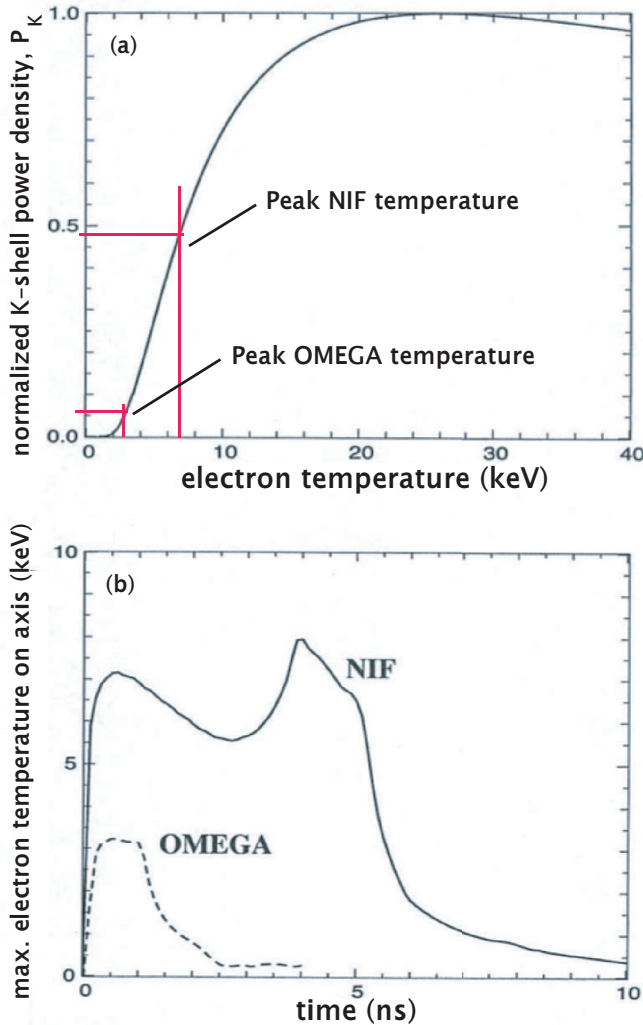
FIG. 4. (Color online) (a) K-shell power density for Kr ions versus electron temperature as given by Eq. (1). (b) Maximum electron temperature on the cylindrical target's axis as given by simulation for NIF and OMEGA-scale targets. Note, the OMEGA pulse is 1 ns long.

where $h\nu$ is the photon energy, and kT_e is the electron temperature. P_K normalized by the peak output K-shell power in the He$_\alpha$ line at $h\nu = 13$ keV as a function of temperature is plotted in Fig. 4(a). The peak output power occurs at the temperature where $(\partial P_K)/\partial(kT_e) = 0$, that is, at $(kT_e)_{\max} = 2h\nu = 26$ keV. Since cooling by adiabatic expansion keeps the temperature in the subcritical density plasma < 10 keV [14], these laser-heated plasmas are always at temperatures $< (kT_e)_{\max}$ for K-shell emitters with atomic number greater than that of Ti or V. Thus, for the Kr plasmas of the present

work, the laser-to-x-ray CE is determined by the steeply rising part of the curve in Fig. 4(a).

The plasma temperature is estimated from detailed simulations. X-ray emission is determined from a non-LTE superconfiguration atomic model, called DCA, that was previously developed and incorporated into the two-dimensional radiation-hydrodynamics code Lasnex [30] by Scott and Hansen [31]. The DCA model solves the rate equations to obtain the populations of each energy level of each ion stage. It is a principal quantum number description that includes 10–20 quantum energy levels per ionization stage. The calculation of line shapes includes Stark, Doppler, and configuration broadening. Electron thermal conduction is treated in the code in the Spitzer-Harm formulation [32] with a flux limiter of 0.2 to account for nonlocal thermal transport.

Figure 4(b) shows the simulated maximum electron temperature on axis (where the hot spot is located) as a function of time for the actual NIF target and for an equivalent OMEGA-scale target. Note that for the NIF target, the peak electron temperature is between 6 and 8 keV for the entire duration of the laser pulse, whereas the peak temperature in the OMEGA plasma is between 2 and 3 keV. Although the power density deposited into the plasma by the laser is about the same for both NIF and Omega—that is, ~ 7 times the power in NIF (140 TW vs 20 TW) is deposited into ~ 8 times the volume (a 4-mm $\times$ 4-mm cylindrical volume vs a 2-mm $\times$ 2-mm cylindrical volume)—the peak temperatures achieved on NIF are ~ 3 times higher than on OMEGA. Finally, substituting these numbers into Eq. (1), we find $P_K(\mathrm{NIF})/P_K(\mathrm{Omega}) \approx 18.5$.

This enhancement in the CE is consistent with the simulations, from which we find CE into > 9 keV photons of 2.1% for the NIF target and 0.09% for the OMEGA target. This enhancement is within a factor of 2 of the measurements discussed above: $\approx 2.9\%$ at NIF (Table I); $\approx 0.3\%$ at OMEGA [17]. Note also that the CE enhancement factor provided by NIF increases with the K-shell photon energy, and is thus much higher for Kr than it is for Fe, for example. At the lower K-shell photon energy for Fe the same analysis leads us to expect an approximate factor of 3 in the enhancement of the CE for the Fe K-shell emission in going from OMEGA to NIF, which is just what was measured in companion experiments to those reported here, and which will be the subject of a future communication.

[1] K. B. Fournier, C. Constantin, J. Poco, M. C. Miller, C. A. Back, L. J. Suter, J. Satcher, J. Davis, and J. Grun, Phys. Rev. Lett. **92**, 165005 (2004).

[2] K. B. Fournier *et al.*, Phys. Plasmas **16**, 052703 (2009).

[3] J. D. Colvin, K. B. Fournier, M. J. May, and H. A. Scott, Phys. Plasmas **17**, 073111 (2010).

[4] F. Pérez *et al.*, Phys. Plasmas **19**, 083101 (2012).

[5] M. Tanabe *et al.*, Appl. Phys. Lett. **93**, 051505 (2008).

[6] F. Girard *et al.*, Phys. Plasmas **12**, 092705 (2005).

[7] D. Babonneau *et al.*, Phys. Plasmas **15**, 092702 (2008).

[8] H.-K. Chung, K. Fournier, and R. Lee, High Energy Density Phys. **2**, 7 (2006).

[9] W. L. Kruer, *The Physics of Laser Plasma Interactions* (Westview Press, Boulder, CO, 2003).

[10] C. A. Back *et al.*, Phys. Rev. Lett. **87**, 275003 (2001).

[11] C. A. Back, J. Davis, J. Grun, L. J. Suter, O. L. Landen, W. W. Hsing, and M. C. Miller, Phys. Plasmas **10**, 2047 (2003).

[12] K. B. Fournier *et al.*, Phys. Plasmas **17**, 082701 (2010).

[13] C. A. Haynam *et al.*, Appl. Opt. **46**, 3276 (2007).

[14] J. D. Colvin, K. B. Fournier, J. Kane, S. Langer, M. J. May, and H. A. Scott, High Energy Density Phys. **7**, 263 (2011).

[15] B. Yaakobi, F. J. Marshall, and R. Epstein, Phys. Rev. E **54**, 5848 (1996).

[16] J. Seely *et al.*, J. Quant. Spectrosc. Radiat. Transf. **99**, 572 (2006).

[17] M. C. Miller, C. A. Back, K. B. Fournier, L. J. Suter, J. Grun, J. F. Seely, and J. F. Davis, UCRL-JC-148517 (unpublished).

[18] T. Boehly *et al.*, Opt. Commun. **133**, 495 (1997).

[19] K. B. Fournier, C. Constantin, C. A. Back, L. Suter, H.-K. Chung, M. C. Miller, D. H. Froula, G. Gregori, S. H. Glenzer, and O. L. Landen, J. Quant. Spectrosc. Radiat. Transf. **99**, 186 (2006).

[20] P. Wegner, J. Auerbach, T. Biesiada, S. Dixit, J. Lawson, J. Menapace, T. Parham, D. Swift, P. Whitman, and W. Williams, in *Optical Engineering At The Lawrence Livermore National Laboratory II: The National Ignition Facility*, Proceedings of the SPIE, edited by M. A. Lane and C. R. Wuest Vol. 5341 (SPIE-Int. Soc. Opt. Eng., 2004), pp. 180–189.

[21] E. L. Dewald *et al.*, Rev. Sci. Instrum. **75**, 3759 (2004).

[22] K. M. Campbell, F. A. Weber, E. L. Dewald, S. H. Glenzer, O. L. Landen, R. E. Turner, and P. A. Waide, Rev. Sci. Instrum. **75**, 3768 (2004).

[23] A. Seifter and G. A. Kyrala, Rev. Sci. Instrum. **79**, 10F323 (2008).

[24] M. J. May, J. R. Patterson, C. Sorce, K. Widmann, K. B. Fournier, and F. Pérez, Rev. Sci. Instrum. **83**, 10E117 (2012).

[25] D. H. Froula *et al.*, Rev. Sci. Instrum. **75**, 4168 (2004).

[26] A. J. Mackinnon *et al.*, Rev. Sci. Instrum. **75**, 4183 (2004).

[27] S. P. Regan *et al.* (unpublished).

[28] M. J. Haugh, S. P. Regan, K. D. Jacoby, P. W. Ross, J. Magoon, M. A. Barrios, J. A. Emig, M. J. Shoup III, and K. B. Fournier, Rev. Sci. Instrum. **83**, 10E122 (2012).

[29] Y. B. Zel'dovich and Y. P. Raizer, *Physics of Shock Waves and High-Temperature Hydrodynamic Phenomena* (Academic, New York, 1967).

[30] G. Zimmerman and W. Kruer, Comments Plasma Phys. Controlled Fusion **2**, 51 (1975).

[31] H. A. Scott and S. B. Hansen, High Energy Density Phys. **6**, 39 (2010).

[32] L. Spitzer, *Physics of Fully Ionized Gases* (Wiley, New York, 1962).